Journal of MATERIALS RESEARCH

Article
DOI: 10.1557/jmr.2019.96

Microstructure and properties of CoCrNi medium-entropy alloy produced by gas atomization and spark plasma sintering

Jianying Wang[1], Hailin Yang[1,a], Jianming Ruan[1], Yun Wang[2], Shouxun Ji[2]

[1]State Key Laboratory of Powder Metallurgy, Central South University, Changsha 410083, China
[2]Institute of Materials and Manufacturing, Brunel University London, Uxbridge, Middlesex UB8 3PH, U.K.
[a]Address all correspondence to this author. e-mail: y-hailin@csu.edu.cn

Received: 3 January 2019; accepted: 20 February 2019

A homogeneous structured CoCrNi medium-entropy alloy was synthesized by gas atomization and spark plasma sintering (SPS). The mechanical properties, corrosion resistance, and magnetic properties were reported in this study. The as-atomized CoCrNi MEA powder, with a spherical morphology in shape and a mean particle diameter of 61 μm, consisted of a single face-centered cubic (FCC) phase with homogeneous distributions of Co, Cr, and Ni elements. Also, the cross-sectional microstructure of powder particles gradually transformed from fully cellular structure into equiaxed-type structure with increasing particle size. After being sintered by SPS, the CoCrNi MEA consisted of a single FCC phase with a mean grain size of 20.8 μm. Meanwhile, the CoCrNi MEA can capable of offering an ultimate tensile strength of 799 MPa, yield strength of 352 MPa, elongation of 53.6%, and hardness of 195.3 HV. In addition, this MEA showed superior corrosion resistance to that of 304 SS (stainless steel) in both 0.5 mol/L HCl and 1 mol/L NaOH solutions. The magnetization loop indicated that this MEA has good soft magnetic properties.

Introduction

High-entropy alloys (HEAs), consisting of at least five equiatomic or near-equiatomic elements crystalized as simple solid solution structures, have attracted significant interest owing to their unique phase structures and superior properties [1, 2, 3, 4, 5]. For example, the typical simple face-centered cubic (FCC) CoCrFeNiMn HEA generally exhibited excellent tensile strength (above 1 GPa) and fracture toughness (exceeding 200 MPa $m^{1/2}$) [6]. The $Al_xCoCrFeNi$ HEAs exhibit superior corrosion resistance compared with that of conventional corrosion-resistant alloys, such as stainless steels and Al, Ni, Ti, and Cu alloys [5]. Nevertheless, the origin of the formation of simple solid solution structures and answer on whether more elements improve the mechanical properties of HEAs are still controversial. The explanation of development of simple solid solution structures rather than intermetallic phases by increasing the number of elements to obtain a higher entropy might be wrong, as demonstrated by related experimental and CALPHAD simulation results [2, 7]. On the other hand, Gail et al. reported that the introduction of Mn to the CoCrFeNi medium-entropy alloy (MEA) had a negligible effect on the degree of solid solution strengthening, as evidenced by their similar yield strength and ultimate tensile strength [8]. Therefore, there was no systematic correlation between mechanical properties and the number of alloying elements.

Considering the above controversial results, MEAs, a similar design approach of HEAs and consisting of two to four equiatomic or near-equiatomic elements, have been presented by recent studies [8, 9, 10]. Particularly, the three-component CoCrNi MEA exhibits a high work hardenability and excellent toughness [11, 12, 13, 14, 15, 16]. Laplanche et al. fabricated a CoCrNi MEA by arc melting and reported that the strength and fracture toughness of the CoCrNi MEA were improved, compared with those of CoCrFeMnNi HEAs [17]. The results indicated that the superior mechanical properties were attributed to twinning activation at higher stress and strain levels. However, the current investigations are seldom focused on the synthesis of the CoCrNi MEA with powder metallurgy (P/M). Generally, the preparation methods of

https://doi.org/10.1557/jmr.2019.96 Published online by Cambridge University Press

© Materials Research Society 2019

HEAs/MEAs by smelting ingots, conventional sintering, and mechanical alloying have distinct disadvantages. For example, HEAs/MEAs synthesized by arc and induction melting have restrictions in processing, associated with the high temperature melting of the ingots and repeated melting to obtain homogeneous compositions [18, 19, 20]. Similarly, HEAs/MEAs produced by mechanical alloying can be easily contaminated by the material milling owing to the longer time of high energy milling. Moravcik et al. prepared CoCrNi powder by mechanical alloying and reported that a large number of oxide phases were formed in the microstructure of CoCrNi MEA owing to the contact of powder with air during the milling process [16].

Among several existing manufacturing processes, gas atomization process is a widely used powder making route that provides good homogeneity, high processing efficiency, and potential for mass production. The unique spherical nature of gas-atomized powder is also preferred for additive manufacturing. For example, CoCrFeNiMn and $Al_xCoCrFeNi$ HEAs have been fabricated by gas atomization and additive manufacturing [21, 22, 23]. Therefore, gas-atomized powders also have potential for additive manufacturing of MEA, such as CoCrNi. In addition, the combination of gas atomization and spark plasma sintering (SPS) could be used to overcome the above fabrication drawbacks owing to the smaller risk of contamination, grain refinement, reduced segregation, etc. To the best of our knowledge, no studies have been reported on investigation of CoCrNi MEA using gas atomization and SPS. Therefore, CoCrNi MEA was produced by combination of gas atomization and SPS in this study. The microstructure and composition of the as-atomized powder and sintered alloy were carefully characterized. Meanwhile, the mechanical properties, corrosion resistance, and magnetic properties of the MEA were systematically investigated and discussed.

Results and discussion

Microstructure and chemical composition analysis of as-atomized CoCrNi MEA powder

Scanning electron microscope (SEM) micrographs and the particle size distribution of gas-atomized CoCrNi MEA powder are shown in Fig. 1. The majority of raw gas-atomized powders had a spherical shape. Satellite particles were observed on the surface of a few powder particles emerged by collisions of large and small powder particles during the flight process in the spray chamber. Additionally, very few powder particles

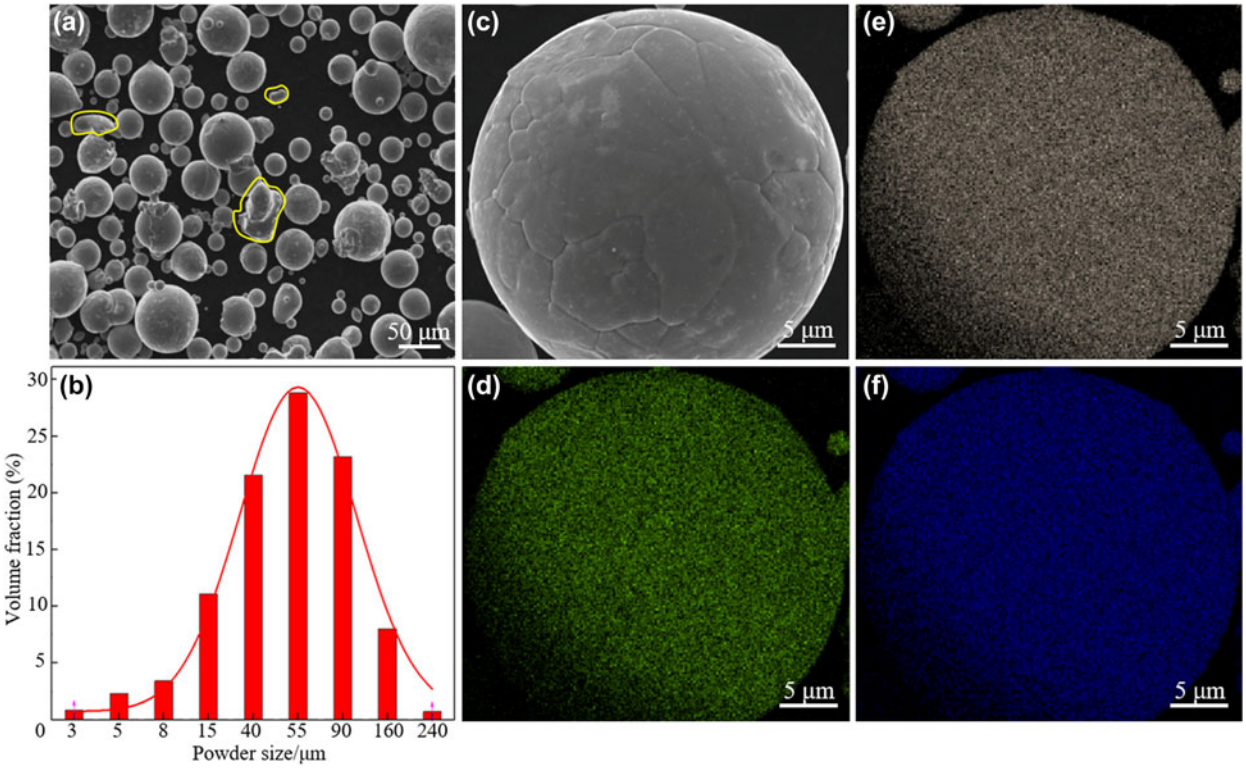


Figure 1: (a) SEM micrograph and (b) particle size distribution of CoCrNi gas-atomized powder. (c)–(f) EDS mapping showing the element distribution of a CoCrNi gas-atomized powder particle.

https://doi.org/10.1557/jmr.2019.96 Published online by Cambridge University Press

© Materials Research Society 2019

were relatively flat with rounded edges, marked by the yellow circles in Fig. 1(a). This is because the spheroidization time of liquid droplets was longer than the solidification time, so that CoCrNi MEA powder was solidified before it was globalized. As shown in Fig. 1(b), the median particle size D_{50} of CoCrNi MEA powder synthesized by gas atomization in this study was approximately 61 μm. In addition, the gas-atomized CoCrNi powder fabricated in this study with high purity, superior sphericity, and fine particle size can be potentially used for additive manufacturing.

Energy-dispersive spectrometer (EDS) mappings of an as-atomized CoCrNi powder particle are shown in Figs. 1(c)–1(f). The results indicated that the Co, Cr, and Ni elements were uniformly distributed in the single-phase solid solution without any composition segregation.

The surface morphologies and cross-sectional microstructure of CoCrNi MEA powder particles with different sizes are shown in Figs. 2(a)–2(f). As shown in Figs. 2(a)–2(c), the surface of as-atomized CoCrNi powder particles became gradually smooth as the diameter decreases. The cross-sectioned morphologies exhibited that an approximately full cellular structure appeared as the particle diameter was approximately 8.0 μm owing to the higher cooling rate. However, the grains gradually transformed from fully cellular structures into equiaxed-type structures with an increase in the particle size, as shown in Figs. 2(e) and 2(f). This could be attributed to the promoted eutectic process brought by decreasing cooling rate.

Microstructure and chemical composition analysis of as-sintered CoCrNi MEA

Figures 3(a) and 3(b) show SEM-BSE (Backscattered Electron) micrographs of CoCrNi MEA. SPSed CoCrNi MEA exhibited a homogenous single phase with a few small pores, as marked by arrows in Fig. 3(a). In addition, annealing twins were observed in the microstructure of CoCrNi MEA after electrolytic polishing [Fig. 3(b)]. The electron backscattered diffraction (EBSD) map with an inverse pole figure (IPF) of CoCrNi MEA is shown in Fig. 3(c). The annealing twins are also clearly visible in the microstructure. The average grain size of the FCC phase was 20.8 μm, which was significantly smaller than the mean particle size of raw as-atomized CoCrNi MEA powder, as shown in Fig. 1(b). This could be attributed to two factors: (i) the larger surface of the powder particles has more than one nucleation particle in the solidification process, as shown in Figs. 2(e) and 2(f); and (ii) the SPS process can inhibit grain growth in the sintering process owing to the fast heating and cooling rate. The IPFs of the FCC phase, shown as insets in Fig. 3(c), confirm that the FCC grains have no obvious preferred orientation in SPSed CoCrNi MEA.

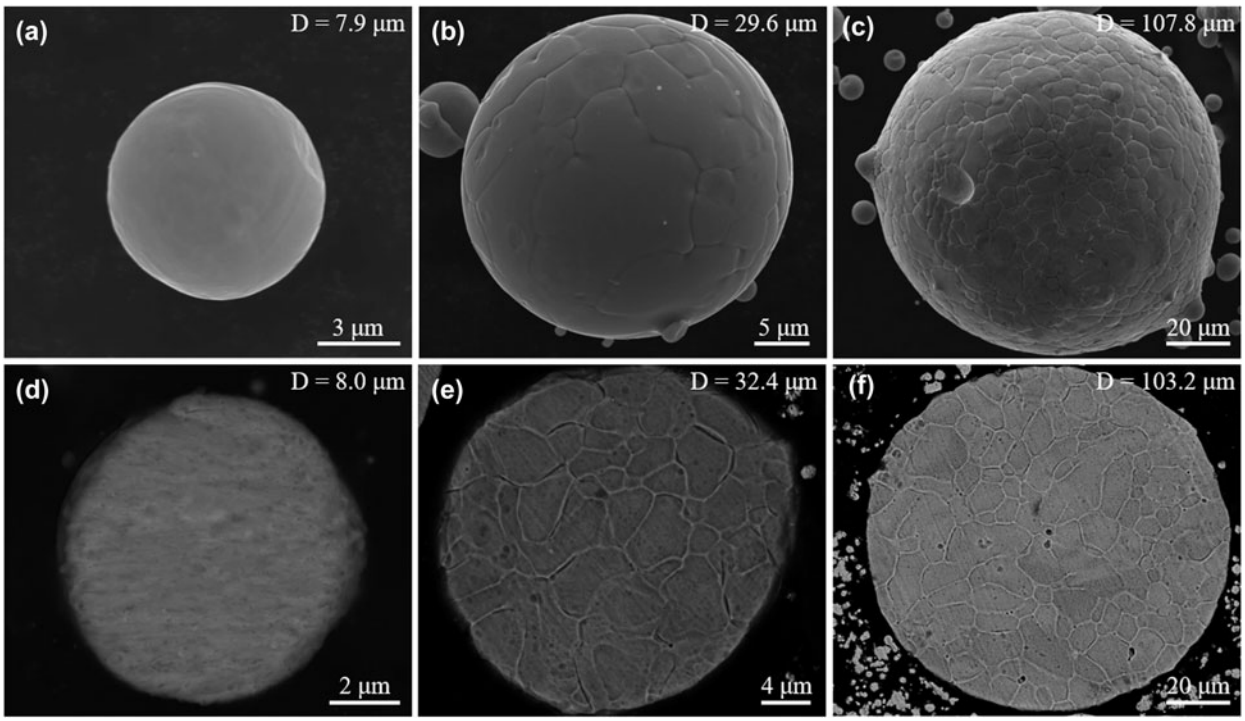


Figure 2: SEM micrographs showing the surfaces for different particle sizes of CoCrNi gas-atomized powder: (a) about 10 μm, (b) about 30 μm, and (c) about 100 μm. Cross-sectioned morphologies of different particle sizes of CoCrNi gas-atomized powder: (d) about 10 μm, (e) about 30 μm, and (f) about 100 μm.

https://doi.org/10.1557/jmr.2019.96 Published online by Cambridge University Press

© Materials Research Society 2019

X-ray diffraction (XRD) spectra of as-atomized CoCrNi MEA powder and SPSed CoCrNi MEA are shown in Fig. 3(d). The results indicated that as-atomized powder has a single-phase FCC structure. After being sintered at a high temperature, CoCrNi MEA also has the single-phase FCC structure with no visible change in the phase composition, which is in good agreement with previous studies [11, 12, 13]. This also demonstrated that no impurities, such as O and C, were introduced.

Further insights into the microstructure are obtained by bright-field (BF) transmission electron microscope (TEM) image, high-resolution TEM (HRTEM), and fast Fourier transform (FFT). Figure 4(a) shows the BF image with a selected-area diffraction pattern from SPSed CoCrNi MEA. The diffraction spot from the L_1 position in the inset of Fig. 4(a) verified that the phase has an FCC structure. The annealing twin phase is also observed in Fig. 4(b). The formation of annealing twins revealed that this CoCrNi MEA has a low stacking fault energy (γ_{SFE}) in the range of 18–45 MJ/m^2 [16]. Corresponding HRTEM image and FFT pattern of twin phase are shown in Fig. 4(c). The results are consistent with the SEM results in Fig. 3. It is also noted that there are no new phases (oxide or carbide) generated, which is in accord with the result of XRD spectrum in Fig. 3(d).

Mechanical properties of SPSed CoCrNi MEA

Figure 5(a) shows the stress–strain curve of SPSed CoCrNi MEA tensile deformed to fracture at room temperature. CoCrNi MEA exhibited yield strength (σ_{YS}) of 352 MPa, ultimate tensile strength (σ_{UTS}) of 799 MPa, total elongation of 53.6%, and Vickers hardness of 195 HV. In addition, the bulk density of CoCrNi MEA tested by the Archimedes method is about 8.26 g/cm^3. The fracture surfaces of the tensile test specimens are shown in Figs. 5(b) and 5(d). A number of dimples with features of typical ductile fractures are observed.

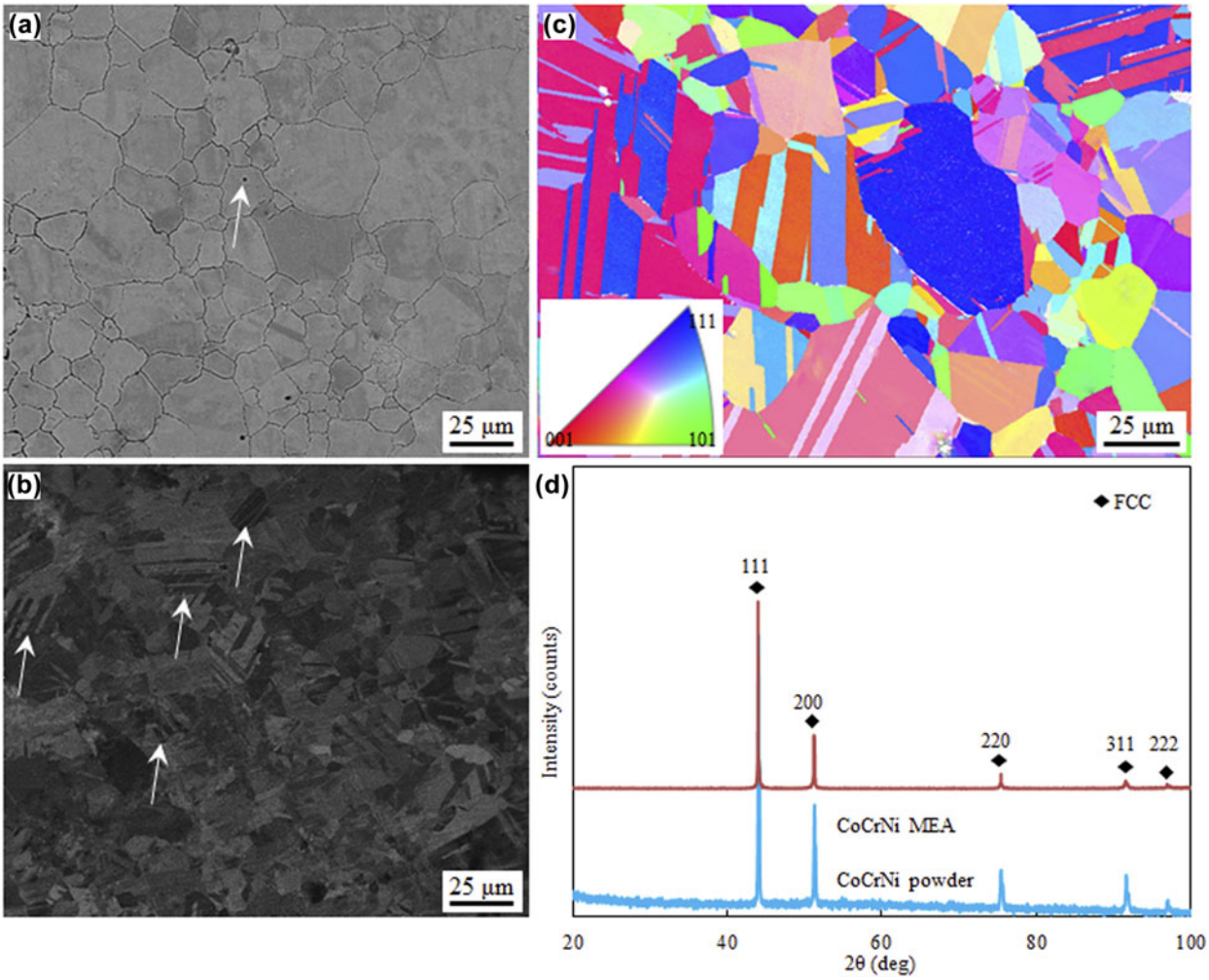


Figure 3: (a) and (b) Backscattered SEM micrographs showing the microstructure of CoCrNi MEA. (c) EBSD mapping of CoCrNi MEA and (d) XRD spectra of CoCrNi gas-atomized powder and SPSed CoCrNi MEA.

https://doi.org/10.1557/jmr.2019.96 Published online by Cambridge University Press

© Materials Research Society 2019

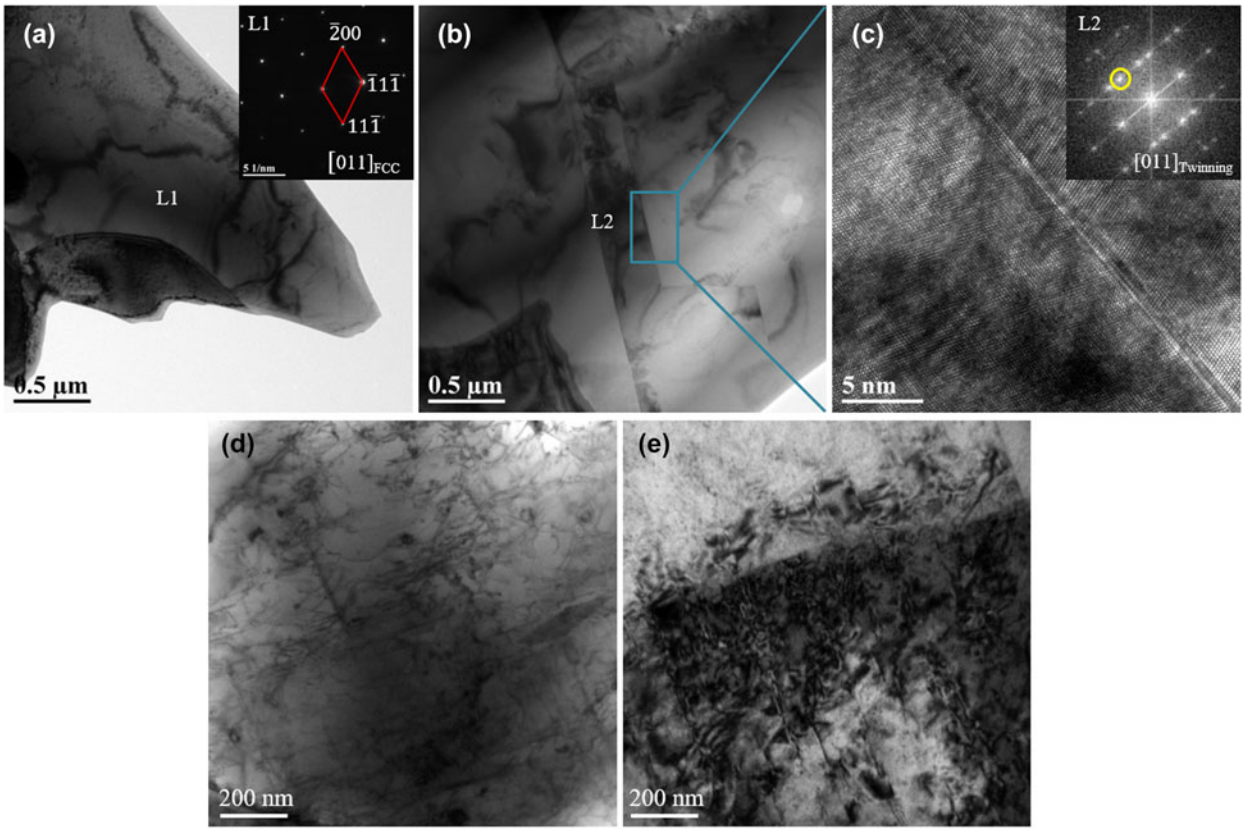


Figure 4: TEM analysis of CoCrNi MEA, including (a) BF and selected-area diffraction pattern showing FCC structure of CoCrNi MEA; (b) and (c) BF, HRTEM, and FFT showing annealing twins; and (d) and (e) TEM BF observations of CoCrNi MEA after tensile deformation.

In Fig. 5(c), the ultimate tensile strength and elongation of CoCrNi MEA alloy analyzed in this study are compared with those of the same MEAs synthesized by other methods [15, 16] and other typical HEAs/MEAs [6, 24, 25, 26, 27]. CoCrNi MEA produced by this combination method of gas atomization and SPS in this study exhibited relatively good ductility but moderate ultimate yield strength.

TEM micrographs of SPSed CoCrNi MEA after the tensile deformation are shown in Figs. 4(d) and 4(e). A high density of dislocations can be observed in CoCrNi MEA, as indicated in Fig. 4(a). Furthermore, some narrow deformation twins in Fig. 4 (b) with a width of tens of nanometers are observed. Therefore, the plastic deformation of CoCrNi MEA was dominantly accommodated by dislocation motion and deformation-induced twinning. Thus, this superior ductility can be attributed to two reasons: one is the combination of gas atomization and SPS methods can deliver fabrication advantages, such as the smaller risk of contamination and grain refinement, and the other is that twin boundaries resulted from nanotwinning provide a steady source of strain hardening by blocking the motion of dislocations.

Magnetic properties of SPSed CoCrNi MEA

Figure 6(a) presents the magnetic hysteresis loop of SPSed CoCrNi MEA measured by the vibrating sample magnetometer (VSM) at room temperature. The saturated magnetization (M_s) and coercivity (H_c) of CoCrNi MEA are approximately 1.70 emu/g and 45.24 Oe, respectively, under a magnetic field of 20,000 Oe, which indicated that the prepared CoCrNi MEA can be capable of having a soft magnetic characteristic. It has been reported that the single-phase FCC FeCoCrNi MEA exhibits a paramagnetic curve with an M_s of 3 emu/g [28]. Ji et al. investigated the magnetic properties of a CoCrFeNiMn HEA prepared by SPS [29]. It is well known that the M_s highly depends on the composition and grain size of the alloy [30, 31]. SPSed CoCrNi MEA has a lower M_s than those of the FeCoCrNi MEA and CoCrFeNiMn HEA, which can be attributed to the higher atomic ratio of Cr (antiferromagnetic element) and larger grain size (20.8 μm).

Corrosion properties of SPSed CoCrNi MEA

Figures 6(b) and 6(c) show representative potentiodynamic polarization curves of SPSed CoCrNi MEA compared with those of a 304 SS in the 0.5 mol/L H_2SO_4 and 1 mol/L NaOH solutions at room temperature. The relevant parameters are summarized in Table I. Based on the electrochemical theory, the more positive free corrosion potential (E_{corr}) and smaller free corrosion current density (I_{corr}) indicate an improved

https://doi.org/10.1557/jmr.2019.96 Published online by Cambridge University Press

© Materials Research Society 2019

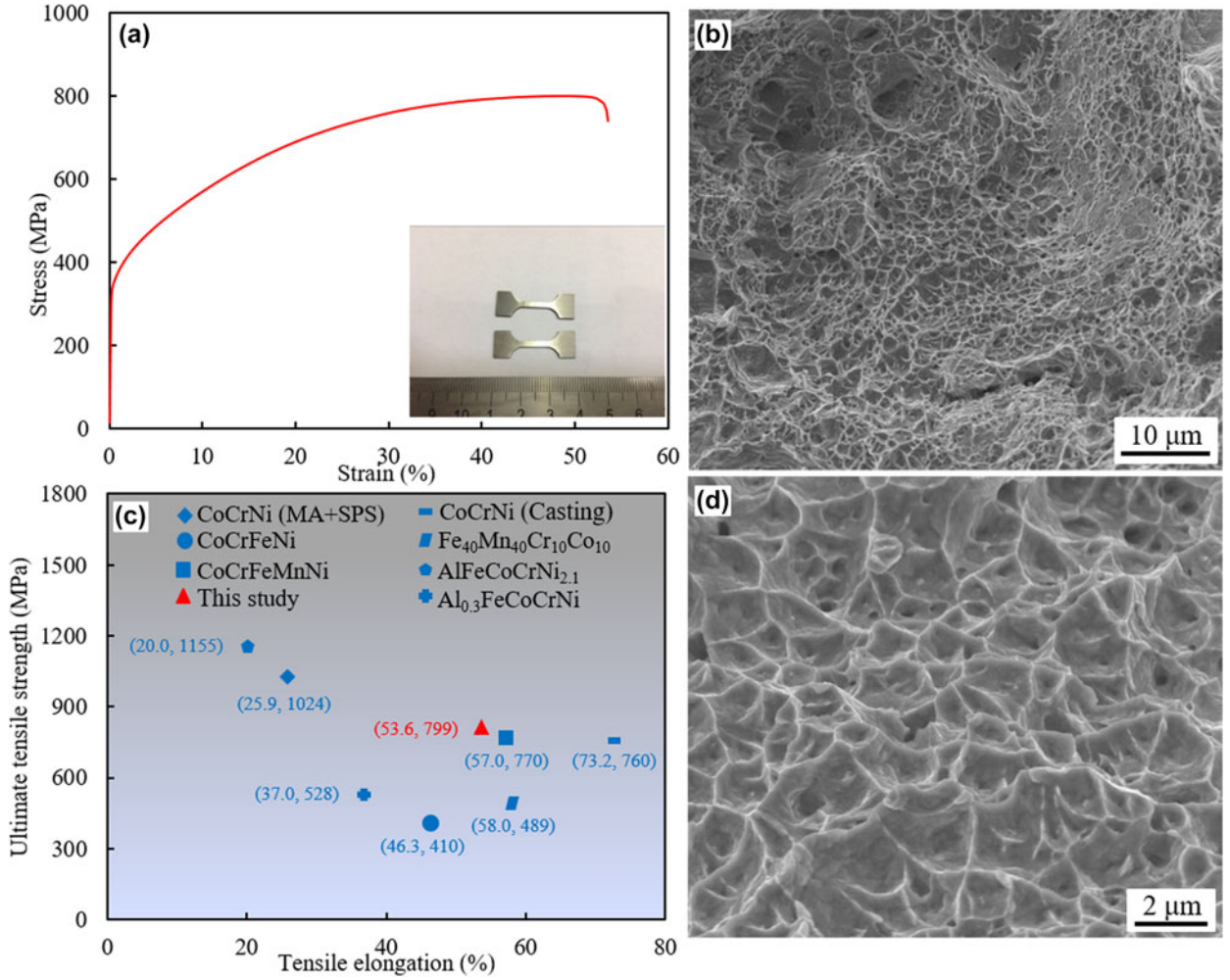


Figure 5: (a) Tensile stress–strain curves of the pure CoCrNi MEA. (b) and (d) Fracture surfaces of as-sintered CoCrNi MEA. (c) Comparison of strength versus deformation of CoCrNi MEA synthesized by other methods [15, 16] and other typical HEA/MEAs [6, 24–27].

corrosion resistance [32, 33]. It is worth noting that compared with the 304 SS, CoCrNi MEA exhibited a higher E_{corr} and lower I_{corr} in both 0.5 mol/L H_2SO_4 and 1 mol/L NaOH solutions. The results indicate that CoCrNi MEA exhibits a superior corrosion resistance to that of the 304 SS in the two different solutions.

Electrochemical impedance spectra (EIS) of CoCrNi MEA and 304 SS in the 0.5 mol/L H_2SO_4 and 1 mol/L NaOH solutions were measured at the open-circuit potential (OCP). The Nyquist and Bode spectra are shown in Fig. 7. The Nyquist spectra show that both specimens exhibit similar features. The capacitive semicircle covers the high-, mid-, and low-frequency regions; the arc radius of CoCrNi MEA is larger than that of the 304 SS. From the Bode spectra of the two kinds of materials in Figs. 7(c) and 7(d), only one time constant is obtained in the two different solutions. In addition, the value of $|Z|$ at a fixed frequency of 0.1 Hz in the Bode spectra usually corresponds to the polarization resistance, which reflects the corrosion resistance of the alloy in the solution [34]. As shown in Figs. 7(c) and 7(d), the values of $|Z|$ at 0.1 Hz for CoCrNi MEA ($\sim 2.293 \times 10^3\ \Omega\ cm^2$ and $1.206 \times 10^3\ \Omega\ cm^2$) are higher than those for 304 SS ($\sim 4.61 \times 10^2\ \Omega\ cm^2$ and $5.75 \times 10^2\ \Omega\ cm^2$) in the 0.5 mol/L H_2SO_4 and 1 mol/L NaOH solutions. Both Nyquist and Bode spectra indicate that the corrosion resistance of CoCrNi MEA is superior to that of the 304 SS. Table II shows the equivalent-circuit parameters of CoCrNi MEA and 304 SS. The R_f (polarization resistance) of CoCrNi MEA is higher than that of 304 SS under the same conditions. This suggests that the applied potential (in the passive region) leads to the formation of stable and protective passive films in the two alloys. The passive films on the surface of CoCrNi MEA are more stable with higher protective abilities compared with the passive films on the surface of 304 SS. These findings are consistent with the above EIS results obtained under OCP conditions.

https://doi.org/10.1557/jmr.2019.96 Published online by Cambridge University Press

© Materials Research Society 2019

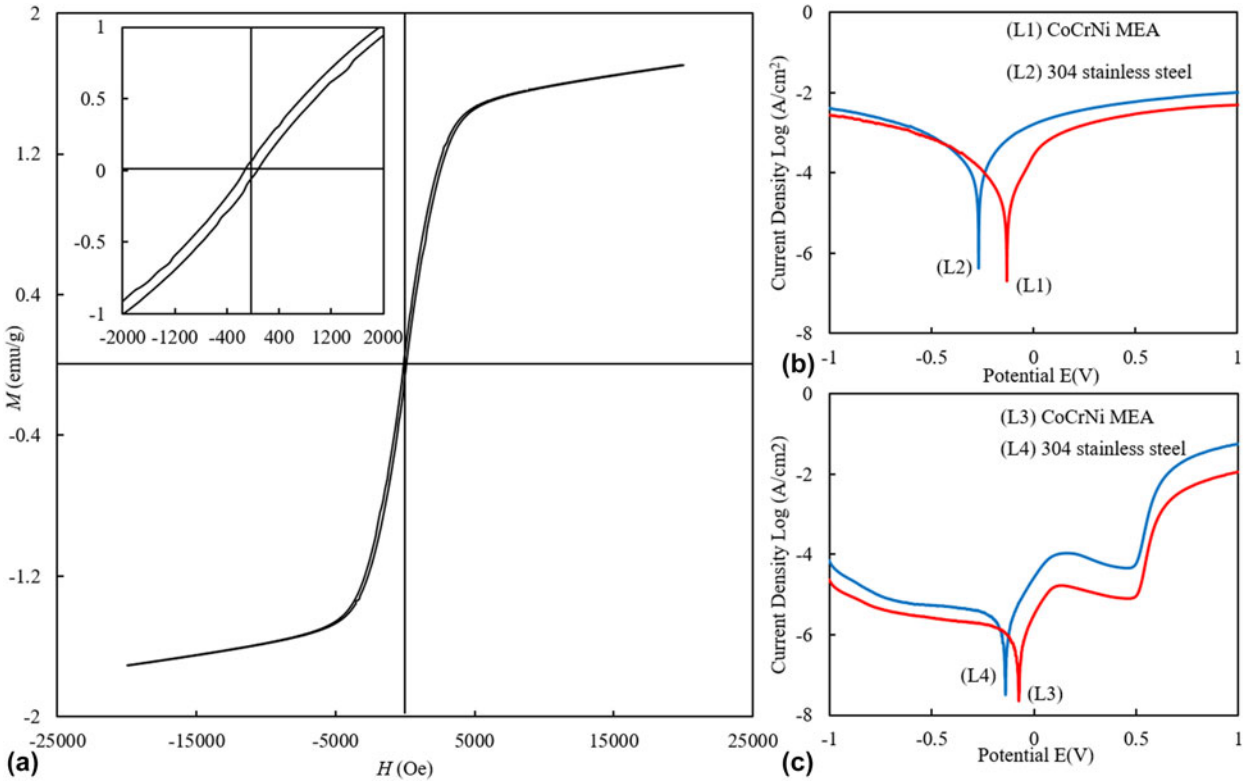


Figure 6: (a) Magnetic hysteresis loops of CoCrNi MEA. Potentiodynamic polarization curves of CoCrNi MEA and 304 SS in the (b) 0.5 mol/L H_2SO_4 and (c) 1 mol/L NaOH solutions.

TABLE I: Electrochemical parameters of potentiodynamic polarization curves.

Sample conditions	Corrosion potential E_{corr} (V versus SCE)	Current density I_{corr} (A/cm^2)
CoCrNi (H_2SO_4)	−0.132	8.285×10^{-6}
304 SS (H_2SO_4)	−0.260	2.592×10^{-4}
CoCrNi (NaOH)	−0.074	5.637×10^{-7}
304 SS (NaOH)	−0.139	4.246×10^{-6}

The surface morphologies of CoCrNi MEA and 304 SS after immersions in the 0.5 mol/L H_2SO_4 and 1 mol/L NaOH solutions are shown in Fig. 8. It can be found that the surfaces were not significantly corroded, which indicates that the two kinds of materials have good corrosion resistances. Figures 8(a) and 8(c) show surface morphologies of CoCrNi MEA after immersions in the 0.5 mol/L H_2SO_4 and 1 mol/L NaOH solutions, respectively. Only a small number of corrosion pits were observed on the surfaces, which suggests that CoCrNi MEA suffered only from localized corrosion. Similarly, Figs. 8(b) and 8 (d) show surface morphologies of 304 SS after immersions in the 0.5 mol/L H_2SO_4 and 1 mol/L NaOH solutions, respectively. After immersion in the 0.5 mol/L H_2SO_4 solution, some corrosion pits were invisible and localized corrosion also occurred at the surface. Figure 8(d) shows that the localized and intergranular corrosions are the major corrosion types of the 304 SS after the immersion in the 1 mol/L NaOH solution.

Conclusions

In this study, CoCrNi MEA was fabricated by gas atomization and SPS. Microstructures, mechanical and magnetic properties, and corrosion resistances were characterized. The main results can be summarized as follows.

(1) As-atomized CoCrNi MEA powder (~61 μm) had a spherical structure with homogeneous distributions of Co, Cr, and Ni. Both as-atomized CoCrNi powder and SPSed CoCrNi MEA consisted of a single-phase FCC.

(2) The surface of the CoCrNi powder becomes gradually smooth as the diameter decreases. With increasing particle size, equiaxed-type structures become the dominate microstructure, which may be attributed to the promoted eutectic process brought by decreasing cooling rate.

(3) CoCrNi MEA exhibited a high tensile yield strength of 352 MPa, ultimate tensile strength of 799 MPa, tensile elongation to fracture of 53.6%, and hardness of 195 HV. The improved mechanical properties can be attributed to the fabrication methods and the formation of deformation twinning.

(4) CoCrNi MEA had a higher M_s (1.70 emu/g) and lower H_c (45.24 Oe), promising for its application as a soft

https://doi.org/10.1557/jmr.2019.96 Published online by Cambridge University Press

© Materials Research Society 2019

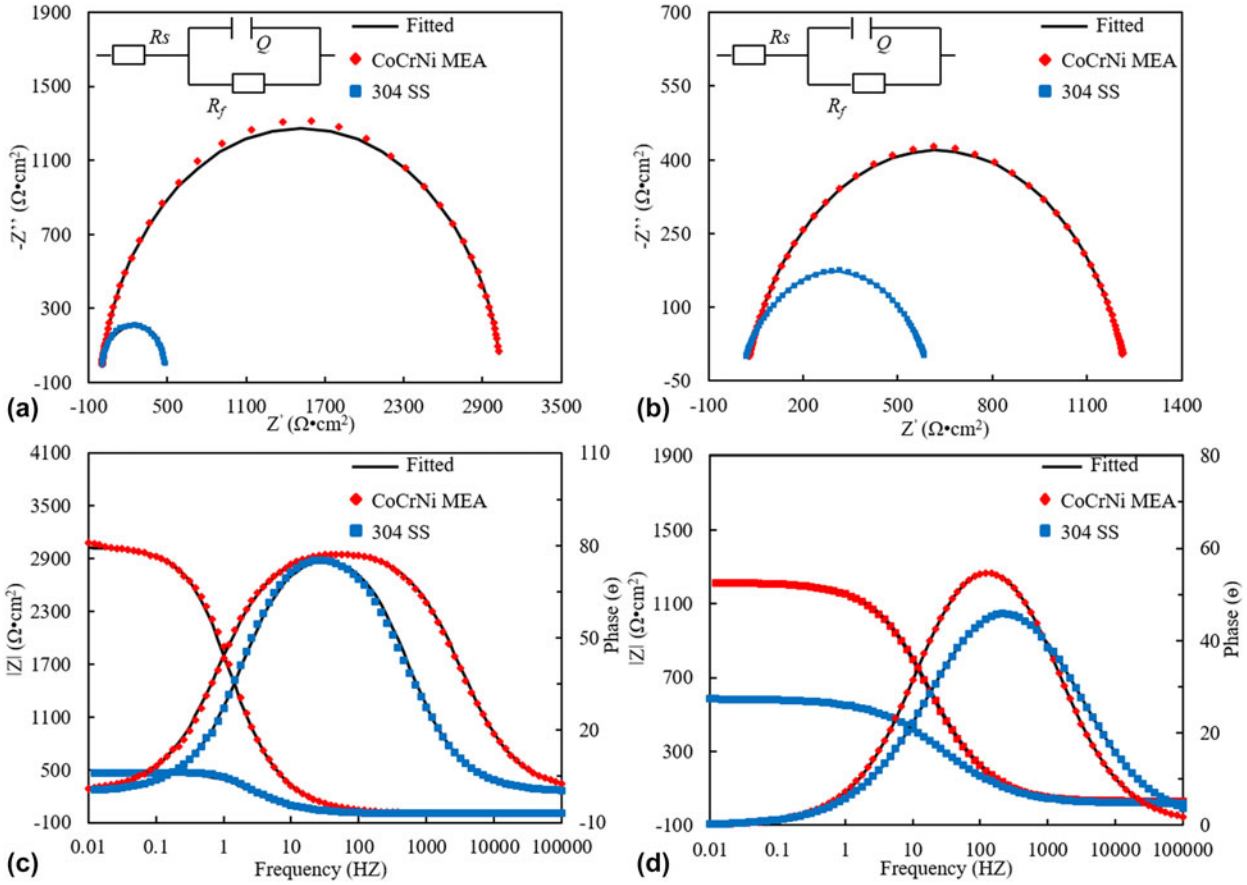


Figure 7: Nyquist and Bode spectra of CoCrNi MEA and 304 SS after immersion in 0.5 mol/L H_2SO_4 solution (a) and (c) and 1 mol/L NaOH solution (b) and (d). (Note: the scattered symbols represent the experimental data and the solid lines represent the fitted results).

TABLE II: Equivalent circuit parameters for impedance spectra of the MEA and 304 SS samples.

Sample conditions	Materials	R_s (Solution resistance) (Ω cm^2)	Q [Ω/(cm^2 s^n)]	R_f (polarization resistance) (Ω cm^2)	$\Sigma\chi^2$
H_2SO_4	MEA	1.913	7.551×10^{-5}	3013	2.228×10^{-3}
	304 SS	4.993	1.126×10^{-4}	478	3.892×10^{-3}
NaOH	MEA	1.534	2.883×10^{-5}	1186	3.853×10^{-3}
	304 SS	1.266	6.311×10^{-5}	565.9	1.764×10^{-3}

magnet. Lower M_s of CoCrNi can be attributed to the higher atomic ratio of Cr (antiferromagnetic element) and larger grain size (20.8 μm).

(5) CoCrNi MEA exhibited superior corrosion resistances to that of the 304 SS in both 0.5 mol/L HCl and 1 mol/L NaOH solutions.

Experimental Procedure

Powder and alloy manufacturing

The composition of the investigated alloy was ternary Co–Cr–Ni, with equal atomic contents of the elements. Element ingots of cobalt, chromium, and nickel were provided by the Beijing Jiaming platinum industry (cobalt >99.98 wt%, chromium >99.2 wt%, and nickel >99.97 wt%). The powder of the same composition was then prepared using the high-pressure nitrogen gas atomization method. The ingots were heated up to the operating temperature (T_m = 1943 K); subsequently, the molten alloy was ejected through a nozzle with a N_2 pressure of 1.8 MPa. This resultant CoCrNi MEA powder was subsequently consolidated by SPS in a graphite die of an inner diameter of 40 mm at 1473 K for 15 min with a heating rate of 100 K/min and a uniaxial pressure of 40 MPa. To limit the exposure to air, as-sintered CoCrNi powder was stored in sealed containers and inserted into the SPS dies under protective Ar atmosphere.

https://doi.org/10.1557/jmr.2019.96 Published online by Cambridge University Press

© Materials Research Society 2019

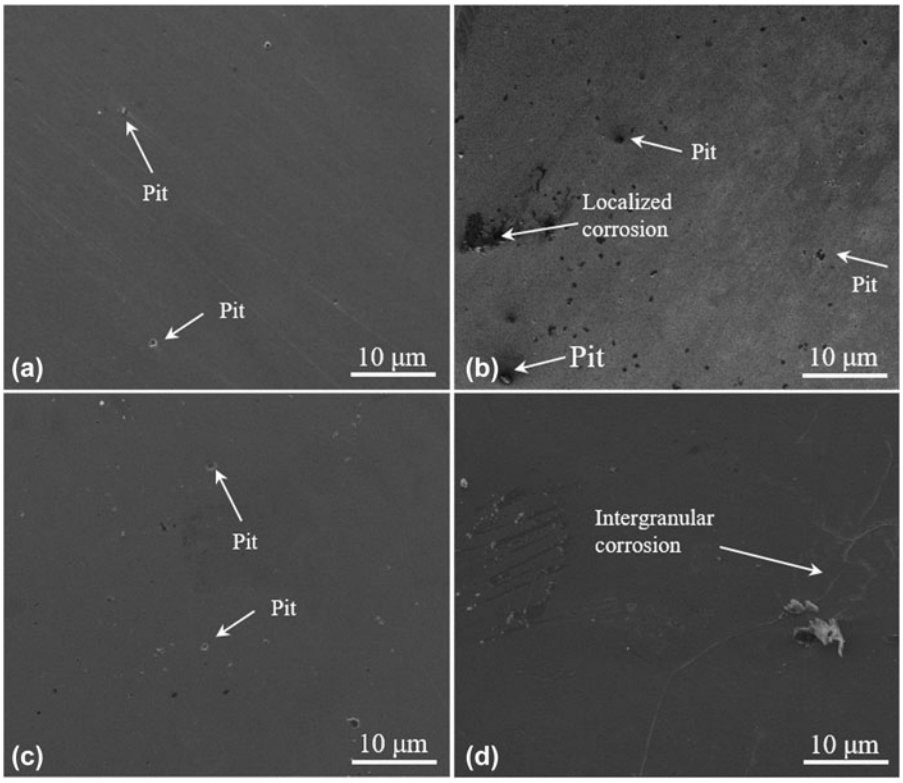


Figure 8: The corrosion morphologies of CoCrNi MEA and 304 SS after immersion in 0.5 mol/L H_2SO_4 solution (a, b) and 1 mol/L NaOH solution (c, d).

Microstructure characterization

The particle size distribution of CoCrNi powder was analyzed by a laser particle size analyzer (Malvern-Mastersizer V3.60, United Kingdom). XRD (Rigaku X-2000, Tokyo, Japan) was utilized to characterize the phase constituents of CoCrNi powder and SPSed CoCrNi MEA at 40 kV and 30 mA with Cu K_α radiation (λ_{ka} = 1.54 Å). An SEM (FEI nano 230 field emission, FEI USA) equipped with an EDS was used to evaluate the surface, cross-sectional microstructure of as-atomized powder and SPSed CoCrNi MEA. CoCrNi powder was embedded, and then, the sample was mechanically polished and etched using 170 mL H_3PO_4 + 10 mL H_2SO_4 + 10 g Cr_2O_3. Furthermore, the grain size and preferred lattice orientation of SPSed CoCrNi MEA were investigated by EBSD using an FEI Quanta FEG 250 field-emission gun scanning electron microscope (FEG-SEM, FEI USA) and analyzed by the TSL OIM Analysis software (TSL USA). Detailed microstructure characterizations were performed using a Tecnai G2 F20 transmission electron microscope (TEM, FEI USA). To prepare thin foils for the TEM analysis, slices cut from SPSed MEA were mechanically ground and cut into discs with a diameter of 3 mm. These discs were then ground to 50 μm in thicknesses and finally ion beam thinned using a Gatan precision ion polishing system (Gatan USA) at a voltage of 5 kV and incident angle in the range of 3–7°.

Evaluation of mechanical properties

Dog bone–shaped specimens with a gauge length of 10 mm and a cross section of 2.2 × 1.5 mm^2 were fabricated by electrical discharge machining for tensile test. Both sides of the specimens were carefully ground to a 2000 grit finish using SiC paper. The uniaxial tensile tests were performed using a material testing system (MTS Alliance RT30, MTS USA) tension machine at room temperature with an engineering strain rate of 1 × 10^{-3} s^{-1}. Vickers hardness was measured on the polished surfaces of CoCrNi MEA samples using an HVS-5 hardness tester at 5 kgf for 10 s. The bulk density of the samples was measured through the Archimedes method (ASTM, B962-13). All the reported data are the average values of at least 5 specimens.

Electrochemical performance and magnetic tests

Potentiodynamic polarization curves in 0.5 mol/L H_2SO_4 and 1 mol/L NaOH solutions were recorded using a CHI604D electrochemical working station. All the electrochemical analyses were carried out using a conventional three-electrode cell with a saturated calomel electrode (SCE) as the reference electrode, platinum plate as the auxiliary electrode, and specimen as the working electrode. The electrochemical measurements were performed at room temperature (300 K).

https://doi.org/10.1557/jmr.2019.96 Published online by Cambridge University Press

© Materials Research Society 2019

Samples with a dimension of 10 × 10 × 2 mm were ground from 400 to 2000 grit SiC paper, sequentially polished with 0.1 μm diamond powder. Subsequently, they were cleaned with deionizer water and alcohol and then dried in cool air. The electrodes used for the electrochemical tests were connected by a wire welded to the back side of the samples and sealed with a curing epoxy resin, leaving only one face with a size of 1 cm^2 exposed to the solution.

The magnetic properties were characterized by a VSM (Lakeshore 7100) at 300 K with a maximum applied field of 2 T, after calibration with a standard sample.

Acknowledgments

This project was financially supported by National Natural Science Foundation of China with No. 51404302.

References

1. **J.W. Yeh, S.K. Chen, S.J. Lin, J.Y. Gan, T.S. Chin, T.T. Shun, C. H. Tsau, and S.Y. Chang**: Nanostructured high-entropy alloys with multiple principal elements: Novel alloy design concepts and outcomes. *Adv. Eng. Mater.* **6**, 299 (2004).
2. **B. Cantor, I.T.H. Chang, P. Knight, and A.J.B. Vincent**: Microstructural development in equiatomic multicomponent alloys. *Mater. Sci. Eng., A* **375**, 213 (2004).
3. **T. Yang, Y.L. Zhao, W.H. Liu, J.J. Kai, and C. Liu**: L_{12}-strengthened high-entropy alloys for advanced structural applications. *J. Mater. Res.* **33**, 2983 (2018).
4. **R.D. Li, P.D. Niu, T.C. Yuan, P. Cao, and C. Chen**: Selective laser melting of an equiatomic CoCrFeMnNi high-entropy alloy: Processability, non-equilibrium microstructure and mechanical property. *J. Alloys Compd.* **746**, 125 (2018).
5. **Y. Shi, L. Collins, R. Feng, C. Zhang, and N. Balke**: Homogenization of Al_xCoCrFeNi high-entropy alloys with improved corrosion resistance. *Corros. Sci.* **133**, 120 (2018).
6. **B. Gludovatz, A. Hohenwarter, D. Catoor, E.H. Chang, and E. P. George**: A fracture-resistant high-entropy alloy for cryogenic applications. *Science* **345**, 1153 (2014).
7. **F. Zhang, C. Zhang, S.L. Chen, J. Zhu, and W.S. Cao**: An understanding of high entropy alloys from phase diagram calculations. *Calphad* **45**, 1 (2014).
8. **A. Gail and E.P. George**: Tensile properties of high- and medium-entropy alloys. *Intermetallics* **39**, 74 (2013).
9. **Z.G. Wu, W. Guo, K. Jin, and J.D. Poplawsky**: Enhanced strength and ductility of a tungsten-doped CoCrNi medium-entropy alloy. *J. Mater. Res.* **33**, 3301 (2018).
10. **J.Y. Wang, H.L. Yang, Z.L. Liu, S.X. Ji, R.D. Li, and J.M. Ruan**: A novel $Fe_{40}Mn_{40}Cr_{10}Co_{10}$/SiC medium-entropy nanocomposite reinforced by the nanoparticles-woven architectural structures. *J. Alloys Compd.* **772**, 272 (2019).
11. **B. Gludovatz, A. Hohenwarter, K.V.S. Thurston, H. Bei, and Z. Wu**: Exceptional damage-tolerance of a medium-entropy alloy CrCoNi at cryogenic temperatures. *Nat. Commun.* **7**, 10602 (2016).
12. **Y.L. Zhao, T. Yang, Y. Tong, J. Wang, and J.H. Luan**: Heterogeneous precipitation behavior and stacking-fault-mediated deformation in a CoCrNi-based medium-entropy alloy. *Acta Mater.* **138**, 72 (2017).
13. **Y. Ma, F. Yuan, M. Yang, P. Jiang, and E. Ma**: Dynamic shear deformation of a CrCoNi medium-entropy alloy with heterogeneous grain structures. *Acta Mater.* **148**, 407 (2018).
14. **J. Miao, C.E. Slone, T.M. Smith, C. Niu, and H. Bei**: The evolution of the deformation substructure in a Ni–Co–Cr equiatomic solid solution alloy. *Acta Mater.* **132**, 35 (2017).
15. **M.P. Agustianingrum, S. Yoshida, N. Tsuji, and N. Park**: Effect of aluminum addition on solid solution strengthening in CoCrNi medium-entropy alloy. *J. Alloys Compd.* **781**, 866 (2019).
16. **I. Moravcik, J. Cizek, Z. Kovacova, J. Nejezchlebova, and M. Kitzmantel**: Mechanical and microstructural characterization of powder metallurgy CoCrNi medium entropy alloy. *Mater. Sci. Eng., A* **701**, 370 (2017).
17. **G. Laplanche, A. Kostka, C. Reinhart, and J. Hunfeld**: Reasons for the superior mechanical properties of medium-entropy CrCoNi compared to high-entropy CrMnFeCoNi. *Acta Mater.* **128**, 292 (2017).
18. **Z. Li, K.G. Pradeep, Y. Deng, D. Raabe, and C.C. Tasan**: Metastable high-entropy dual-phase alloys overcome the strength–ductility trade-off. *Nature* **534**, 227 (2016).
19. **J. Wang, T. Guo, J. Li, W. Jia, and H. Kou**: Microstructure and mechanical properties of non-equilibrium solidified CoCrFeNi high entropy alloy. *Mater. Chem. Phys.* **210**, 192 (2018).
20. **J.B. Seol, J.W. Bae, Z. Li, J.C. Han, and J.G. Kim**: Boron doped ultrastrong and ductile high-entropy alloys. *Acta Mater.* **151**, 366 (2018).
21. **Y. Chew, G.J. Bi, Z.G. Zhu, F.L. Ng, and F. Weng**: Microstructure and enhanced strength of laser aided additive manufactured CoCrFeNiMn high entropy alloy. *Mater. Sci. Eng., A* **744**, 137 (2019).
22. **Z.G. Zhu, Q.B. Nguyen, F.L. Ng, X.H. An, X.Z. Liao, and P. K. Liaw**: Hierarchical microstructure and strengthening mechanisms of a CoCrFeNiMn high entropy alloy additively manufactured by selective laser melting. *Scr. Mater.* **154**, 20 (2018).
23. **J. Joseph, P. Hodgson, T. Jarvis, X.H. Wu, and N. Stanford**: Effect of hot isostatic pressing on the microstructure and mechanical properties of additive manufactured Al_xCoCrFeNi high entropy alloys. *Mater. Sci. Eng., A* **733**, 59 (2018).
24. **W. Hao, H. Zhou, F. Fang, X. Hu, and Z. Xie**: Strain-rate effect upon the tensile behavior of CoCrFeNi high-entropy alloys. *Mater. Sci. Eng., A* **689**, 366 (2017).
25. **Y. Deng, C.C. Tasan, K.G. Pradeep, H. Springer, and A. Kostka**: Design of a twinning-induced plasticity high entropy alloy. *Acta Mater.* **94**, 124 (2015).

https://doi.org/10.1557/jmr.2019.96 Published online by Cambridge University Press

© Materials Research Society 2019

26. **T. Bhattachajee, R. Zheng, Y. Chong, S. Sheikh, and S. Guo**: Effect of low temperature on tensile properties of $AlCoCrFeNi_{2.1}$ eutectic high entropy alloy. *Mater. Chem. Phys.* **210**, 207 (2018).
27. **D. Li, C. Li, T. Feng, Y. Zhang, and G. Sha**: High-entropy $Al_{0.3}CoCrFeNi$ alloy fibers with high tensile strength and ductility at ambient and cryogenic temperatures. *Acta Mater.* **123**, 285 (2017).
28. **M.S. Lucas, L. Mauger, J.A. Munoz, and Y. Xiao**: Magnetic and vibrational properties of high-entropy alloys. *J. Appl. Phys.* **109**, 299 (2011).
29. **W. Ji, W. Wang, H. Wang, J. Zhang, and Y. Wang**: Alloying behavior and novel properties of CoCrFeNiMn high-entropy alloy fabricated by mechanical alloying and spark plasma sintering. *Intermetalllics* **56**, 24 (2015).
30. **Y. Zhang, T.T. Zuo, Y.Q. Cheng, and P.K. Liaw**: High-entropy alloys with high saturation magnetization, electrical resistivity, and malleability. *Sci. Rep.* **3**, 1455 (2013).
31. **A.Z. Arsad and N.B. Ibrahim**: Temperature-dependent magnetic properties of YIG thin films with grain size less 12 nm prepared by a sol–gel method. *J. Magn. Magn. Mater.* **15**, 70 (2018).
32. **X.W. Qiu, Y.P. Zhang, and C.G. Liu**: Effect of Ti content on structure and properties of $Al_2CrFeNiCoCuTi_x$ high-entropy alloy coatings. *J. Alloys Compd.* **585**, 282 (2014).
33. **X.W. Qiu, Y.P. Zhang, L. He, and C.G. Liu**: Microstructure and corrosion resistance of AlCrFeCuCo high entropy alloy. *J. Alloys Compd.* **549**, 195 (2013).
34. **C.A.D. Rovere, J.H. Alano, R. Silva, P.A.P. Nascente, and J. Otubo**: Characterization of passive films on shape memory stainless steels. *Corros. Sci.* **57**, 154 (2012).

https://doi.org/10.1557/jmr.2019.96 Published online by Cambridge University Press

© Materials Research Society 2019